scientific reports

Check for updates

OPEN

First-principles investigation of thermoelectric transport in the two-dimensional Sn_4Sb_8 monolayer

Raphael M. Tromer[1], Isaac M. Felix[2], Georges D. A. Nze[3], Fábio L. L. Mendonça[3] & Marcelo L. Pereira Junior[3]✉

Thermoelectric materials play a crucial role in energy conversion technologies by enabling the direct transformation of heat into electricity, offering a promising route for sustainable energy harvesting. This study investigates the thermoelectric properties of the two-dimensional Sn_4Sb_8 monolayer using first-principles calculations within the density functional theory (DFT) framework, combined with Boltzmann transport theory. We systematically compute the electrical conductivity, Seebeck coefficient, and electronic contribution to thermal conductivity using the BoltzTraP code. At the same time, the relaxation time is determined via an Arrhenius approach, enabling the estimation of absolute transport coefficients. The lattice thermal conductivity is also obtained through a semi-empirical method that accounts for phonon contributions. The thermoelectric figure of merit (*ZT*) is evaluated across various chemical potentials and temperatures, revealing strong anisotropy between the *x* and *y* transport directions. At room temperature ($T = 300$ K), the maximum *ZT* values reach 0.5 for electrons and 0.35 for holes. As the temperature increases, the thermoelectric efficiency improves, with the highest *ZT* reaching 0.81 for electrons along the *x* direction at $T = 900$ K. At the same time, hole transport becomes nearly isotropic with $ZT = 0.72$ in both directions. These results establish Sn_4Sb_8 as a strong candidate for thermoelectric applications, demonstrating significant efficiency from ambient to high temperatures. The material's favorable transport properties and high *ZT* values make it an excellent prospect for energy conversion technologies. Future research should focus on experimental validation and potential optimizations through strain engineering and doping strategies to enhance performance.

Keywords Two-dimensional systems, Thermoelectric properties, Physical properties, Density functional theory

Two-dimensional (2D) materials have been extensively studied due to their electromechanical, electronic, and thermal properties, making them promising candidates for various nanotechnological applications[1,2]. In particular, their high surface-to-volume ratio and strong electronic confinement allow for precise manipulation of their properties, rendering them highly attractive for devices and emerging technologies[3] in electronics[4], photovoltaics[5], sensing[6], and other fields[7]. In the energy transition context, thermoelectric materials have garnered significant interest due to their ability to directly convert waste heat into electricity, contributing to energy efficiency and sustainability efforts[8–10]. Consequently, investigating and developing new thermoelectric materials can substantially impact recovering wasted energy from industrial processes and enhancing renewable energy generation, thereby reducing dependence on fossil fuels[11].

From a thermoelectric perspective, 2D materials offer remarkable advantages, as the reduced dimensionality can decrease lattice thermal conductivity[12] while simultaneously improving electronic transport[13], both crucial factors for optimizing thermoelectric performance[14–16]. This phenomenon arises, among other factors, due to enhanced phonon scattering in low-dimensional structures, effectively suppressing unwanted thermal dissipation[17]. Additionally, these systems exhibit characteristic vibrational modes known as flexural phonons, which play a fundamental role in further reducing thermal conductivity[18]. The ability to engineer these materials' structural and chemical properties further enables fine-tuning their electronic characteristics to maximize thermoelectric efficiency[14]. As a result, the search for novel 2D materials with high thermoelectric potential has become a key focus of theoretical and computational research[19,20].

[1]Institute of Physics, University of Brasília, Brasília, DF, Brazil. [2]Center for Agri-food Science and Technology, Federal University of Campina Grande, Pombal, PB, Brazil. [3]College of Technology, Department of Electrical Engineering, University of Brasília, Brasília, DF, Brazil. ✉email: marcelo.lopes@unb.br

The use of high-performance computational approaches has driven recent advancements in material discovery. The study conducted by Lyngby and Thygesen employed a crystal diffusion variational autoencoder (CDVAE) to predict novel 2D materials, significantly expanding the known space of stable structures[21]. Their model was trained on a dataset of 2,615 2D materials with formation energies up to 0.3 eV/atom above the convex hull, generating 10,000 new materials, among which 8,599 were identified as potentially stable. Moreover, 2,004 of these structures exhibited formation energies within 50 meV/atom above the convex hull, suggesting a high likelihood of experimental synthesis[21]. These newly predicted materials were incorporated into the Computational 2D Materials Database (C2DB)[22], making them accessible for further investigations.

Among the materials predicted through this approach, some monolayers were subsequently analyzed in theoretical studies focused on thermoelectric transport. For instance, CdBr, CdI, and Janus Cd_2BrI were examined by Wu *et al.*, who reported significant electrical conductivity and Seebeck coefficient values, in addition to reduced thermal conductivity[23]. Their study highlighted the thermoelectric potential of theoretically predicted 2D materials; however, it represented only a tiny fraction of the vast material space identified by Lyngby and Thygesen[21].

Complementarily, IV-VI 2D compounds, such as SnS and SnSe, were investigated by Shafique and Shin, revealing the considerable figure of merit (ZT) values across different temperatures and crystallographic directions, demonstrating that Sn-containing structures can exhibit competitive thermoelectric performance[24]. Among the various nanomaterials studied by Lyngby and Thygesen, Sn_4Sb_8 – a two-dimensional material with AB_2 stoichiometry and an energy above the convex hull of 0.02 eV/atom – has not yet been investigated in the literature regarding its electronic and thermal transport properties, leaving its viability for thermoelectric applications an open question.

In this work, we investigate the thermoelectric properties of Sn_4Sb_8 through calculations based on density functional theory (DFT) and Boltzmann transport theory. We analyze its electronic and structural properties, including band structure and electronic density of states, and key thermoelectric transport parameters such as Seebeck coefficient, electrical conductivity, and electronic thermal conductivity, computed using the Boltzmann Transport Properties (BoltzTraP) software within the relaxation time approximation. Additionally, we assess its anisotropic characteristics, reflected in directional variations in transport behavior. The lattice thermal conductivity and relaxation time were determined based on well-established methodologies, allowing the thermoelectric ZT to be computed. Our results indicate that Sn_4Sb_8 exhibits a ZT of approximately 0.8 at temperatures of 600 and 900 K, a competitive value among 2D thermoelectric materials, highlighting its potential for thermal-to-electric energy conversion applications.

Results and discuss

The structure investigated in this study was selected from the C2DB database[22,25] and corresponds to the stoichiometry Sn_4Sb_8, also referred to by its structural formula $SnSb_2$. Tin-based compounds (Sn) are widely recognized for their promising thermoelectric properties, attributed to the combination of high electrical conductivity and intrinsically low thermal conductivity. In particular, Sn_4 Sb_8 exhibits a moderate band gap, suggesting that it can maintain favorable thermoelectric performance even at relatively low temperatures.

Moreover, when considering all Sn-containing monolayers available in the C2DB database (Sb_2, Sb_4, Sn_4, SnSb, Sn_2, Sn_4Sb_8, Sn_6Sb_2), Sn_4Sb_8 exhibits the lowest energy above the convex hull, with $\Delta H_{\mathrm{hull}} = 0.02$ eV/atom[25]. This result indicates that this structure has the highest thermodynamic stability among the considered compositions, implying a greater feasibility for experimental synthesis.

Although the Sn_4Sb_8 system investigated here, whose simplified stoichiometry corresponds to $SnSb_2$, has not yet been reported in the experimental literature, it exhibits structural and electronic features that are closely related to those of established thermoelectric materials such as $SnSb_2Te_4$[26], $SnTe_2$[27], and Sb_2Te_3[28]. In particular, the relaxed structure of Sn_4Sb_8 presents a layered arrangement and anisotropic bonding patterns similar to the directionally bonded frameworks found in these chalcogenide systems.

First-principles calculations confirm the dynamical and thermodynamic stability of the compound under standard simulation conditions, with no imaginary phonon modes and a negative formation energy[22,25]. The lack of experimental reports may be attributed to the possible metastable character of this compound or to synthetic challenges, such as phase competition in the Sn-Sb binary system and the tendency of antimony-rich compounds to form complex polymorphs or undergo phase segregation. Despite these challenges, the predicted transport properties, including high Seebeck coefficients and anisotropic power factors, indicate that Sn_4Sb_8 may represent a viable chalcogen-free analogue within the thermoelectric material landscape. These characteristics suggest that it could be stabilized under non-equilibrium synthesis conditions, such as molecular beam epitaxy[29] or high-pressure techniques[30], which have been successful in accessing layered phases beyond the thermodynamic ground state.

The nanomaterial crystallizes in an orthorhombic configuration and belongs to the $PM2_1B$ symmetry group, with a cohesive energy (E_{coh}) of -1.91 eV/atom, calculated using the expression $E_{\mathrm{coh}} = (E_{Sn_4Sb_8} - 4E_{\mathrm{Sn}} - 8E_{\mathrm{Sb}})/12$, where $E_{Sn_4Sb_8}$ is the total energy of the monolayer, E_{Sn} and E_{Sb} are the energies of isolated Sn and Sb atoms, respectively, and 12 represents the total number of atoms in the unit cell of Sn_4Sb_8. Furthermore, no intrinsic magnetization was observed in this structure. Figure 1 presents the optimized atomic structure of Sn_4Sb_8 from different perspectives, highlighting the unit cell.

Structural analysis reveals the presence of two predominant chemical bonds, Sn-Sb and Sb-Sb, with bond lengths of 2.87 Å and 2.91 Å, respectively. The in-plane lattice parameters of the optimized geometry are $a = 4.35$ Å and $b = 11.48$ Å. In contrast, the out-of-plane lattice parameter is $c = 30.0$ Å, with $\alpha = \beta = \gamma = 90.0^\circ$, indicating orthorhombic symmetry. Although the system is modeled directly as an isolated monolayer, its geometric thickness, measured as the vertical distance between the outermost atoms, is approximately 6.85 Å. The larger value of the c parameter arises from the inclusion of a vacuum layer along the z-axis, a standard procedure in

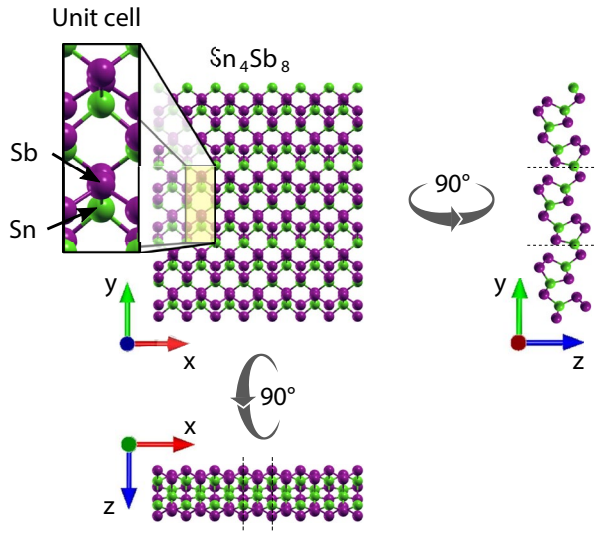

Fig. 1. Top and side views of the atomic structure of the Sn_4Sb_8 monolayer. The unit cell is highlighted, illustrating the arrangement of Sn (green) and Sb (purple) atoms. The left panel presents the top view, while the upper and right panels display side views obtained by rotating the structure by 90° along the *x*- and *y*-axes, respectively.

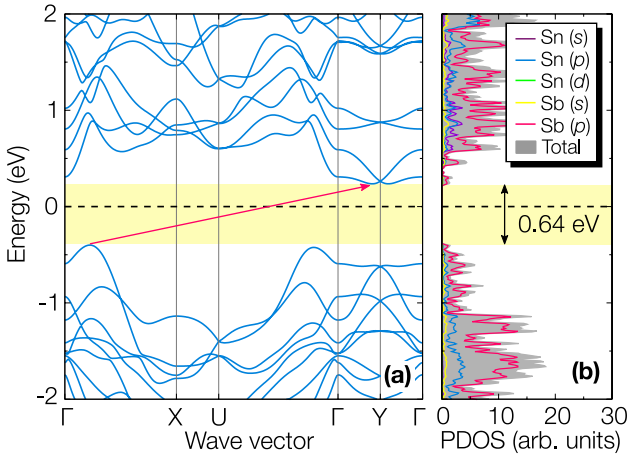

Fig. 2. (**a**) Electronic band structure of Sn_4Sb_8 along high-symmetry points in the Brillouin zone. The dashed line represents the Fermi level, and the highlighted yellow region indicates the band gap. The arrow marks a transition between the valence and conduction bands. (**b**) Projected density of states showing the contributions of Sn and Sb atomic orbitals. The shaded area corresponds to the total density of states.

first-principles simulations of two-dimensional materials, which aims to suppress spurious interactions between periodic images and ensure a proper description of an isolated monolayer.

In Fig. 2, we present the electronic band structure and the projected density of states (PDOS) along the high-symmetry points of the unit cell: $\Gamma = (0.0, 0.0, 0.0)$, $X = (0.5, 0.0, 0.0)$, $U = (0.5, 0.5, 0.0)$, and $Y = (0.0, 0.5, 0.0)$. The analysis of the band structure confirms that Sn_4Sb_8 is a semiconductor with an indirect bandgap, where the valence band maximum (VBM) is located at Γ and the conduction band minimum (CBM) at Y. The calculated bandgap is 0.64 eV, a relevant value for thermoelectric applications due to its potential operation at relatively low temperatures.

The band dispersion exhibits significant variations along different directions in the Brillouin zone. Most bands are dispersive, which is favorable for electronic transport and charge carrier mobility. Although some segments near the valence band maximum, particularly between the Γ and Y points, show reduced dispersion, they are not flat in the strict sense. These moderately dispersive features may contribute to an increased density of states near the Fermi level, potentially enhancing the Seebeck coefficient while preserving reasonable mobility.

Regarding the PDOS, the *p* orbitals of Sb are the primary contributors to electronic conduction, dominating both the valence and conduction bands. The *p* orbitals of Sn also contribute, particularly near the Fermi level. The *d* orbitals of Sn have a negligible impact, indicating that electronic correlation effects are minimal. The overlap

between the electronic states of Sb and Sn suggests a degree of hybridization that enhances band dispersion and promotes electronic transport, further reinforcing the thermoelectric potential of Sn_4Sb_8.

The electronic transport properties were described as functions of temperature (T) and chemical potential (μ), utilizing the energy-dependent conductivity tensor $\sigma_{ij}(\epsilon)$ in conjunction with the Fermi-Dirac distribution function f_0. This framework's chemical potential is inherently linked to the voltage applied across the material. The transport coefficients, including electrical conductivity (σ), Seebeck coefficient (S), and electronic thermal conductivity (κ), were determined through the following expressions:

$$\sigma_{ij}(T,\mu) = \frac{1}{\Omega}\int \bar{\sigma}_{ij}(\epsilon)\left[\frac{-\partial f_0(T,\epsilon,\mu)}{\partial\epsilon}\right]d\epsilon, \tag{1}$$

$$S_{ij}(T,\mu) = \frac{1}{eT\Omega\sigma_{ij}(T,\mu)}\int \bar{\sigma}_{ij}(\epsilon)(\epsilon-\mu)\left[\frac{-\partial f_0(T,\epsilon,\mu)}{\partial\epsilon}\right]d\epsilon, \tag{2}$$

and

$$\kappa_{ij}^{ele}(T,\mu) = \frac{1}{e^2T\Omega}\int \bar{\sigma}_{ij}(\epsilon)(\epsilon-\mu)^2\left[\frac{\partial f_0(T,\epsilon,\mu)}{\partial\epsilon}\right]d\epsilon, \tag{3}$$

where Ω denotes the unit cell volume, e represents the elementary charge, and i, j correspond to Cartesian indices. The transport coefficients, $\sigma_{ij}(T,\mu)$ and $\kappa^{ele}(T,\mu)$, were obtained under the assumption of a constant relaxation time τ within the RTA framework.

Additionally, the lattice thermal conductivity (κ_L) and relaxation time (τ) were evaluated following the methodologies previously established by our group[31,32]. The thermoelectric figure of merit (ZT) was calculated using:

$$ZT = \frac{\sigma S^2 T}{(\kappa_L + \kappa_e)}, \tag{4}$$

where T represents the absolute temperature.

The transport properties were examined within the relaxation time approximation (RTA) framework, considering an isotropic model in which transport characteristics remain direction-independent and electronic band dispersion remains unaltered. The σ, the electronic contribution to thermal conductivity (κ_e), and the Seebeck coefficient were computed using the BoltzTraP code[33].

To obtain the thermoelectric properties, we employed the electronic band structure of Sn_4Sb_8 (see Fig. 2) as input for the BoltzTraP software. This software solves the Boltzmann transport equation by interpolating the electronic bands under the constant relaxation time approximation. The transport coefficients, including electrical conductivity, the Seebeck coefficient, and the electronic contribution to thermal conductivity, were analytically determined as described in the methodology section.

The Seebeck coefficient is obtained in absolute units since the constant relaxation time approximation is adopted. In contrast, the electrical and thermal conductivities are expressed regarding the relaxation time parameter. These coefficients are measured in units of $(\Omega m\ s)^{-1}$ and W/mKs, retaining the time unit (s) associated with the relaxation time. Consequently, to obtain absolute values for the electrical conductivity and the electronic component of thermal conductivity, it is necessary to express the relaxation time as a function of temperature and apply it to the transport parameters.

The electrical conductivity was calculated using the BoltzTraP software. Based on these results, an Arrhenius plot was then constructed for $\mu = 0.0$ eV. The relaxation time was subsequently extracted from this plot following the methodology described in Reference[31]. In this context, Fig. 3(a) presents the electrical conductivity as a function of temperature along the x and y directions, assuming $\mu = 0.0$ and constant relaxation time. The Sn_4Sb_8 system exhibits pronounced anisotropy in electronic transport, with the electrical conductivity along the x direction being significantly higher than in the y direction. This difference is associated with a considerably higher electronic mobility along the x direction, reflecting the material's intrinsic structural characteristics. The stronger interaction between atomic sites in the Sn_4Sb_8 structure along the x direction compared to the y direction further contributes to this behavior (see Fig. 1).

At zero chemical potential ($\mu = 0.0$ eV), the increase in electrical conductivity along the x-direction with temperature can be attributed to enhanced thermal excitation of charge carriers. As the temperature rises, more electrons are thermally promoted from the valence to the conduction band, leading to a higher carrier concentration and, consequently, increased electrical conductivity. This behavior is typical in semimetallic or narrow-gap materials, where thermal activation has a significant influence on transport properties. In contrast, the observed decrease in lattice thermal conductivity with increasing temperature is primarily due to intensified phonon-phonon scattering. At elevated temperatures, the phonon population increases, which enhances the probability of Umklapp scattering processes. These events reduce the phonon mean free path and thus suppress the lattice thermal conductivity. This temperature-dependent decline is a well-known characteristic of crystalline systems, particularly in low-dimensional materials, where phonon transport is strongly affected by anharmonic interactions.

Additionally, the inset of Fig. 3(a) presents the Arrhenius plot for each component of the electrical conductivity tensor. The linearity of the data confirms the thermally activated behavior of electrical conductivity, which is characteristic of semiconductors.

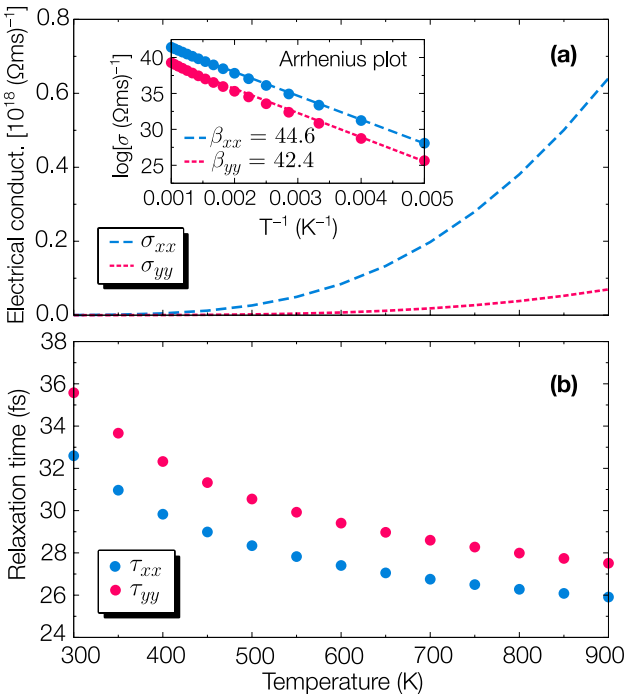

Fig. 3. (**a**) Electrical conductivity as a function of temperature along the x and y directions for the Sn_4Sb_8 monolayer, assuming a chemical potential of $\mu = 0.0$ and constant relaxation time. The inset presents the Arrhenius plot of the electrical conductivity components, from which the linear coefficients β_{xx} and β_{yy} are obtained. (**b**) Relaxation time as a function of temperature for both transport directions, highlighting the anisotropic behavior of the system.

The slope of the angular fit λ allows for the estimation of the material's energy bandgap, given by $E_{\text{band gap}} = -2\kappa_B\lambda$, where κ_B is the Boltzmann constant. A bandgap value of approximately 0.6 eV was obtained, consistent with the value derived from the electronic band structure (see Fig. 2).

The coefficients β_{xx} and β_{yy}, which correspond to the linear coefficients of the Arrhenius fit for each component, are also essential for determining the electronic relaxation time τ. The relaxation time is computed using the following equation:

$$\tau(T) = \frac{\Gamma(T_0)}{\Gamma(T)} \frac{\log\left(\Gamma(T_0)\right)}{\log\left(\Gamma^{\text{Ref}}(T_0)\right)} \tau^{\text{Ref}}(T_0), \tag{5}$$

where T_0 is the reference temperature used for fitting, τ^{Ref} represents a relaxation time previously calculated for a similar system, and $\Gamma(T)$ is an auxiliary function defined as:

$$\Gamma(T) = \log\left(\frac{\sigma(T)}{\beta}\right). \tag{6}$$

Based on this approach, using the estimated values of the linear coefficients $\beta_{xx} = 44.6$ and $\beta_{yy} = 42.4$, and given that the method requires a reference relaxation time from a similar system, we adopted $\tau(300) = 29.4$ fs from the SnSe system[34]. Furthermore, the auxiliary function was determined as $\Gamma^{\text{Ref}}(300) = 32.79$. Thus, we derived the relaxation time expression as a temperature function for the x and y directions, as illustrated in Fig. 3(b). The relaxation time decreases with increasing temperature, a behavior expected due to enhanced phonon scattering[31]. The difference in relaxation times between the x and y directions reinforces the influence of the material's anisotropic structure on its electronic and thermal transport mechanisms.

Once the relaxation time was obtained as a function of temperature, we multiplied the electrical conductivity and the electronic thermal conductivity component by τ at the same temperature value. In Fig. 4, we present: (a) the electrical conductivity σ, (b) the electronic part of thermal conductivity, (c) the Seebeck coefficient, and (d) the power factor $S^2\sigma$, as functions of chemical potential, which is related to hole concentration (negative potential) and electron concentration (positive potential).

From Fig. 4(a), we observe that, similarly to the case of zero chemical potential, i.e., in the absence of excess charge carriers, the transport tensors exhibit anisotropy along the x and y directions. Within the chemical potential range from -2 to 2 eV, the conductivity along the x direction is consistently higher than along the y direction. For holes, the conductivity in the x direction exhibits two maxima around 2.0×10^6 $(\Omega\,\text{m})^{-1}$ at -1.2 eV and -1.9 eV, while in the y direction, a peak of approximately 1.0×10^6 $(\Omega\,\text{m})^{-1}$ appears at -1.6 eV.

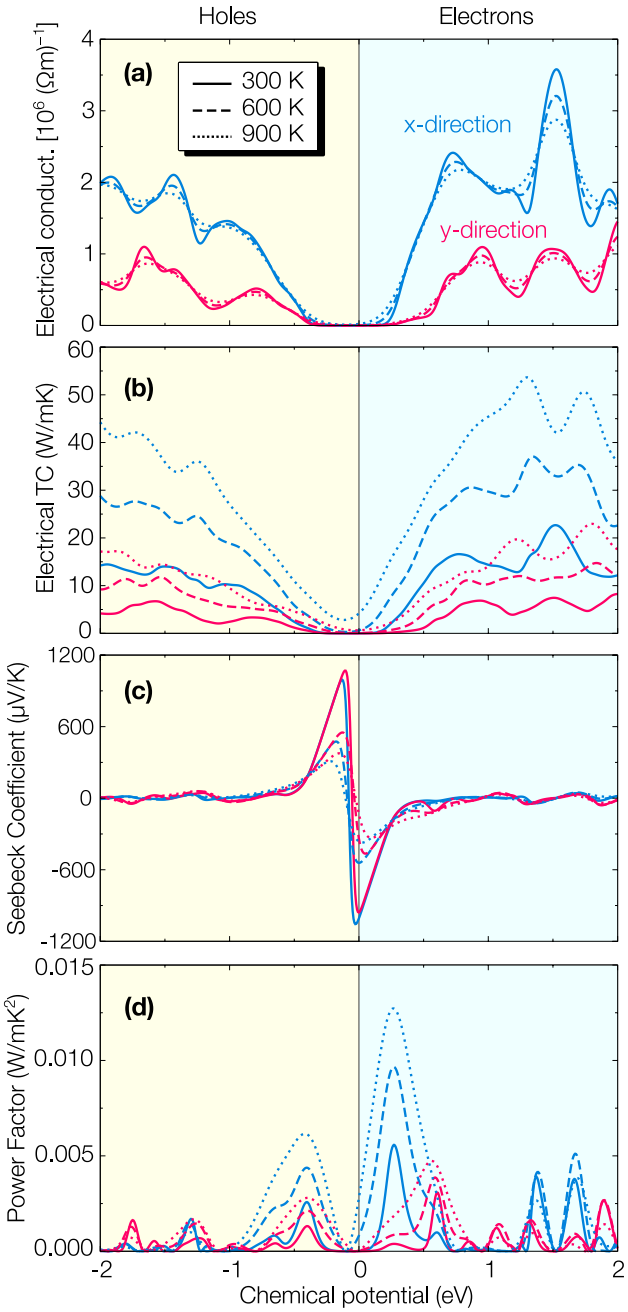

Fig. 4. Electronic transport properties of the Sn_4Sb8 function of components potential at different temperatures (300 K, 600 K, and 900 K). The results are presented for the *x* (blue) and *y* (red) transport directions. (**a**) Electrical conductivity, (**b**) electronic thermal conductivity, (**c**) Seebeck coefficient, and (**d**) power factor. The shaded regions indicate the hole (left) and electron (right) doping regimes.

For electrons, the conductivity peak in the *x* direction occurs at 3.5×10^6 $(\Omega\ \mathrm{m})^{-1}$ at 1.6 eV, whereas in the *y* direction, the maximum reaches approximately 1.4×10^6 $(\Omega\ \mathrm{m})^{-1}$ at 2.0 eV.

It is also noteworthy that temperature influences electrical conductivity. We find that increasing temperature negatively impacts conductivity by examining the peak conductivity values for electrons and holes. For instance, the electron transport peak at $\mu = 1.6$ eV decreases from 3.5×10^6 to 2.8×10^6 $(\Omega\ \mathrm{m})^{-1}$ as temperature increases, which aligns with the fact that charge accumulation rises with temperature, creating a barrier for further carrier injection into the conduction band.

Figure 4(b) presents the electronic contribution to thermal conductivity. Although peak asymmetries are less pronounced than those observed in electrical conductivity, the maximum value still corresponds to electron carriers rather than holes. A key distinction is that temperature enhances electronic thermal conductivity, which negatively affects thermoelectric performance, highlighting the importance of selecting nanomaterials with moderate band gaps for such applications. Furthermore, according to the thermoelectric figure of merit

equation 4, an increase in electronic thermal conductivity reduces ZT, indicating that higher temperatures lower thermoelectric efficiency.

Continuing the analysis, Fig. 4(c) shows the Seebeck coefficient for hole and electron transport. The plot reveals a maximum near the Fermi level, crucial for charge transport. Additionally, there is an asymmetry in the peak positions, with the peak associated with electrons being closer to the Fermi level, thus contributing more significantly to electronic transport. Notably, the Seebeck coefficient reaches a maximum value slightly above 1000 μV/K, characteristic of highly efficient thermoelectric materials[35,36].

Finally, Fig. 4(d) presents the power factor (σS^2), which quantifies the efficiency of purely electronic thermoelectric conversion. The power factor tensor also exhibits strong anisotropy between the directions of x and y. The highest conversion efficiency for holes occurs at $\mu = -0.3$ eV, while for electrons, the peaks are around $\mu = 0.2$ eV. Additionally, we observe that conversion efficiency increases significantly with temperature for both types of carriers. Overall, purely electronic thermoelectric conversion is more efficient for electrons, with a peak efficiency of approximately 0.013 W/mK^2 for electrons and 0.006 W/mK^2 for holes at 900 K.

It is worth noting that the most significant variations in the transport properties, namely electrical conductivity, thermal conductivity, Seebeck coefficient, and power factor, occur within the chemical potential range of approximately -1 eV to $+1$ eV. This behavior stems from the underlying electronic structure, particularly the proximity of this window to the band edges. In this region, the DOS exhibits sharp features, and small shifts in the chemical potential can substantially alter the carrier distribution and their transport contributions. Moreover, at finite temperature, the Fermi-Dirac distribution broadens, but states far from the Fermi level contribute less significantly due to lower occupation probabilities or reduced group velocities. As a result, the -1 to $+1$ eV window encompasses the most transport-active regime of the material and corresponds to realistic doping levels that can be experimentally achieved. This explains the concentration of peak values and key trends in this range across all transport tensors.

To determine the overall Sn_4Sb_8 monolayer thermoelectric conversion efficiency, we incorporate thermal effects by dividing the power factor by the sum of the lattice thermal conductivity arising from phonons and the electronic contribution. This leads to the figure of merit ZT, which quantifies the system's total efficiency. This calculation requires an additional transport property, the lattice thermal conductivity due to phonons (κ_L).

In this study, we adopt a semi-empirical approach based on fitting an Arrhenius expression, where the slope coefficient α provides a vibrational parameter defined as $E_{\mathrm{VIB}} = -2\kappa_B\alpha$, with κ_B being the Boltzmann constant, characterizing the average phonon motion[32]. Within this framework, the thermal conductivity at $T = 300$ K is determined using the following expression:

$$\kappa_L(300) = \frac{\bar{\nu} \times E_{\mathrm{VIB}}}{L \times \delta}, \tag{7}$$

where $\bar{\nu}$ represents the average phonon frequency, L is the lattice parameter, and δ is a free parameter adjusted for a system similar to the one under investigation. All calculations within this approximation were performed using the MOPAC16 software[37], which employs a semi-empirical approach with PM7 parameterization[38].

To calibrate the free parameter δ, we used the thermal conductivity components of SnSe, which are reported as 2.5 W/mK and 2.0 W/mK along the x and y directions, respectively. To reproduce these values, we determined that the free parameter values should be set to 6.5 K and 8 K for the x and y directions, respectively. Applying these calibrated values to the system investigated in this work, we obtained thermal conductivity values at $T = 300$ K of $\kappa_{L,xx} = 1.12$ W/mK and $\kappa_{L,yy} = 0.91$ W/mK.

To obtain the thermal conductivity curve as a function of temperature, we assumed that most 2D materials in the literature exhibit a temperature dependence that follows approximately $\sim T^{-1}$ (insert references). In Fig. 5, we present the lattice thermal conductivity as a function of temperature along the x and y directions,

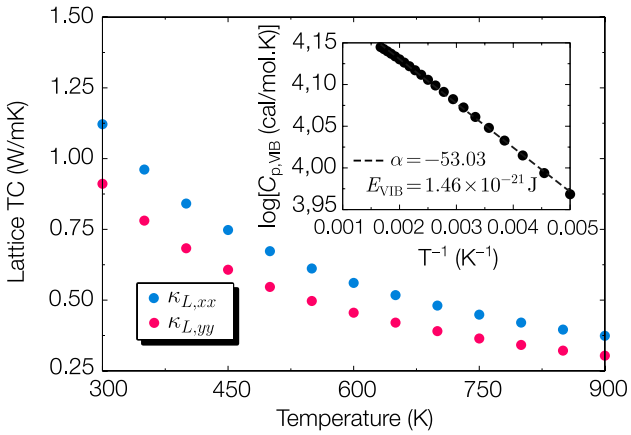

Fig. 5. Lattice thermal conductivity as a function of temperature along the x and y directions for the Sn_4Sb_8 monolayer. The inset presents the Arrhenius plot used to determine the vibrational parameter E_{VIB}, which characterizes the average phonon motion and is crucial in estimating κ_L.

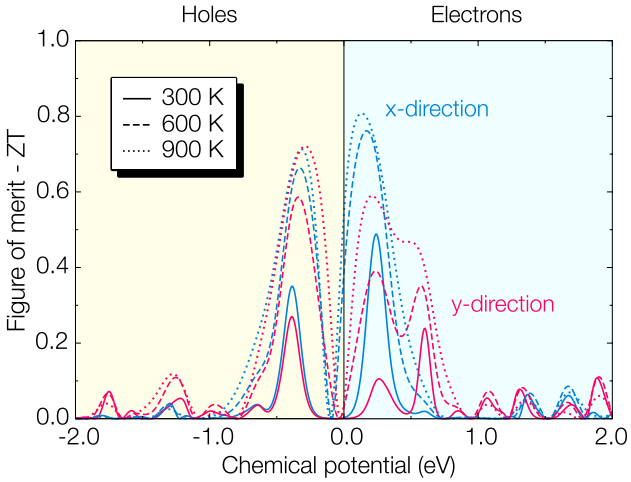

Fig. 6. Thermoelectric figure of merit (ZT) as a function of chemical potential for the Sn_4Sb_8 monolayer along the x and y transport directions, considering both hole (negative chemical potential) and electron (positive chemical potential) transport. The shaded regions indicate the hole-doped (left) and electron-doped (right) regimes.

demonstrating a degree of anisotropy. The inset panel displays the Arrhenius plot used to determine the vibrational parameter.

Once all necessary transport parameters were obtained, we calculated the thermoelectric efficiency using the figure of merit ZT, as defined in Equation 4. The evaluation of ZT was performed over a range of chemical potentials from -2 eV to 2 eV, considering both hole and electron transport along the x and y directions. Figure 6 presents ZT as a function of chemical potential.

For the Sn_4Sb_8 system, ZT exhibits anisotropy between the x and y directions, as expected from the previously discussed transport parameters. Another relevant observation is that the highest efficiency occurs near the Fermi level for holes and electrons, within the chemical potential range of -0.7 eV to 0.8 eV. At room temperature ($T = 300$ K), the efficiency along the x direction is 0.35 for holes and 0.5 for electrons. In contrast, along the y direction, ZT reaches 0.28 for holes and 0.26 for electrons, indicating a significant thermoelectric effect even at room temperature, without requiring an external heat source.

As the temperature increases to $T = 600$ K, a general enhancement in thermoelectric efficiency is observed. In the x direction, ZT values increase to 0.68 for holes and 0.78 for electrons, while in the y direction, values of 0.59 and 0.39 are obtained for holes and electrons, respectively. This trend continues at an even higher temperature of $T = 900$ K, with ZT values in the x direction reaching 0.72 for holes and 0.81 for electrons. Meanwhile, in the y direction, ZT is 0.72 for holes and 0.59 for electrons.

At $T = 900$ K, ZT becomes isotropic for hole transport, with both x and y directions exhibiting a value of 0.72. However, moderate anisotropy persists for electron transport, with values of 0.81 and 0.59 along the x and y directions, respectively. Additionally, ZT appears to saturate in the x direction for both charge carrier types, whereas, in the y direction, further increases may still be possible beyond $T = 900$ K.

For the two-dimensional Sn_4Sb_8 system investigated in this study, the highest thermoelectric efficiency for holes occurs in the x and y directions, with a ZT value of 0.72. In contrast, the highest efficiency is along the x direction for electrons, with a peak ZT of 0.81. These results suggest that Sn_4Sb_8 is a strong candidate for thermoelectric applications over a wide temperature range, from room to high-temperature regimes.

Methodology

The structural and electronic properties of the two-dimensional Sn_4Sb_8 monolayer were explored using DFT as implemented in the Quantum ESPRESSO (QE) software[39]. The calculations were carried out within a plane-wave pseudopotential framework, adopting the generalized gradient approximation (GGA) with the Perdew-Burke-Ernzerhof (PBE) exchange-correlation functional[40].

Structurally optimization was performed to determine the equilibrium geometry by minimizing the total energy and atomic forces, alongside optimizing the stress tensor. A plane-wave energy cutoff of 70 Ry was employed to ensure numerical accuracy, with the atomic forces converging to below 0.01 eV/Å. A vacuum spacing of approximately 23 Å was applied along the out-of-plane (z) direction to prevent spurious interactions due to periodic boundary conditions. The electronic structure calculations, including the band structure and projected density of states, utilized a Monkhorst-Pack k-point grid of $18 \times 18 \times 1$.

Summary and conclusions

This study investigated the thermoelectric properties of the two-dimensional Sn_4Sb_8 monolayer using first-principles calculations combined with Boltzmann transport theory. Our results reveal that the material exhibits a moderate indirect bandgap and pronounced anisotropy in electronic and thermal transport properties.

The computed thermoelectric figure of merit, ZT, indicates that Sn_4Sb_8 achieves high thermoelectric efficiency, particularly at elevated temperatures. At $T = 900$ K, the maximum ZT values reach 0.72 for holes in the x and y directions and 0.81 for electrons along the x direction. These results position Sn_4 Sb_8 as a strong candidate for thermoelectric applications across a broad temperature range, from room temperature to high-temperature regimes.

Moreover, we observe that transport anisotropy diminishes with increasing temperature, particularly for hole transport, where ZT becomes nearly isotropic at $T = 900$ K. Additionally, the saturation trend in ZT at high temperatures along the x direction suggests enhanced thermal stability, which is advantageous for thermoelectric applications requiring long-term operational reliability.

Overall, our findings establish Sn_4Sb_8 as a promising material for thermoelectric energy conversion, offering a well-balanced combination of high electrical conductivity, moderate thermal conductivity, and a strong Seebeck response. All results reported in this work are theoretical predictions based on first-principles and Boltzmann transport calculations. Experimental synthesis and validation remain essential future steps. Future studies should also explore optimization strategies, such as strain engineering and doping, to further enhance the thermoelectric performance of this material.

Data availability

The datasets utilized and/or examined throughout the present study are accessible upon reasonable request from the corresponding author.

Received: 9 June 2025; Accepted: 9 October 2025
Published online: 17 November 2025

References

1. Khan, K. et al. Recent developments in emerging two-dimensional materials and their applications. *J. Mater. Chem. C* **8**, 387–440. https://doi.org/10.1039/C9TC04187G (2020).
2. Kanahashi, K., Pu, J. & Takenobu, T. 2D materials for large-area flexible thermoelectric devices. *Adv. Energy Mater.* **10**, 1902842. https://doi.org/10.1002/aenm.201902842 (2020).
3. Butler, S. Z. et al. Progress, challenges, and opportunities in two-dimensional materials beyond graphene. *ACS Nano* **7**, 2898–2926. https://doi.org/10.1021/nn400280c (2013).
4. Das, T. & Ahn, J.-H. Development of electronic devices based on two-dimensional materials. *FlatChem* **3**, 43–63. https://doi.org/10.1016/j.flatc.2017.05.001 (2017).
5. Wang, H. et al. Recent advances in two-dimensional photovoltaic devices. *J. Semicond.* **45**, 051701. https://doi.org/10.1088/1674-4926/45/5/051701 (2024).
6. Varghese, S. S., Varghese, S. H., Swaminathan, S., Singh, K. K. & Mittal, V. Two-dimensional materials for sensing: graphene and beyond. *Electronics* **4**, 651–687. https://doi.org/10.3390/electronics4030651 (2015).
7. Kaul, A. B. Two-dimensional layered materials: Structure, properties, and prospects for device applications. *J. Mater. Res.* **29**, 348–361. https://doi.org/10.1557/jmr.2014.6 (2014).
8. Baskaran, P. & Rajasekar, M. Recent trends and future perspectives of thermoelectric materials and their applications. *RSC Adv.* **14**, 21706–21744. https://doi.org/10.1039/D4RA03625E (2024).
9. Zhu, T. et al. Compromise and synergy in high-efficiency thermoelectric materials. *Adv. Mater.* **29**, 1605884. https://doi.org/10.1002/adma.201605884 (2017).
10. Snyder, G. J. & Toberer, E. S. Complex thermoelectric materials. *Nat. Mater.* **7**, 105–114. https://doi.org/10.1038/nmat2090 (2008).
11. Singh, R. et al. Advancements in thermoelectric materials for efficient waste heat recovery and renewable energy generation. *Hybrid Adv.* 100176, https://doi.org/10.1016/j.hybadv.2024.100176 (2024).
12. Wang, Y., Xu, N., Li, D. & Zhu, J. Thermal properties of two dimensional layered materials. *Adv. Funct. Mater.* **27**, 1604134. https://doi.org/10.1002/adfm.201604134 (2017).
13. Fiori, G. et al. Electronics based on two-dimensional materials. *Nat. Nanotechnol.* **9**, 768–779. https://doi.org/10.1038/nnano.2014.207 (2014).
14. Han, H. et al. Advancements in thermoelectric materials: optimization strategies for enhancing energy conversion. *J. Mater. Chem. A* **12**, 24041–24083. https://doi.org/10.1039/D4TA03666B (2024).
15. Li, D. et al. Recent progress of two-dimensional thermoelectric materials. *Nano-Micro Lett.* **12**, 1–40. https://doi.org/10.1007/s40820-020-0374-x (2020).
16. Tromer, R. M. et al. Electronic, optical and thermoelectric properties of boron-doped nitrogenated holey graphene. *Phys. Chemi. Chem. Phys.* **22**, 21147–21157. https://doi.org/10.1039/D0CP02869J (2020).
17. Kalantari, M. H. & Zhang, X. Thermal transport in 2D materials. *Nanomaterials* **13**, 117. https://doi.org/10.3390/nano13010117 (2022).
18. Jiang, J.-W., Wang, B.-S., Wang, J.-S. & Park, H. S. A review on the flexural mode of graphene: lattice dynamics, thermal conduction, thermal expansion, elasticity and nanomechanical resonance. *J. Phys.: Condens. Matter* **27**, 083001, https://doi.org/10.1088/0953-8984/27/8/083001 (2015).
19. Kaur, K., Khandy, S. A., Dhiman, S., Sharopov, U. B. & Singh, J. Computational prediction of thermoelectric properties of 2D materials. *Electron. Struct.* **4**, 023001. https://doi.org/10.1088/2516-1075/ac635b (2022).
20. Kozinsky, B. & Singh, D. J. Thermoelectrics by computational design: Progress and opportunities. *Annu. Rev. Mater. Res.* **51**, 565–590. https://doi.org/10.1146/annurev-matsci-100520-015716 (2021).
21. Lyngby, P. & Thygesen, K. S. Data-driven discovery of 2D materials by deep generative models. *npj Comput. Mater.* **8**, 232, https://doi.org/10.1038/s41524-022-00923-3 (2022).
22. Haastrup, S. et al. The computational 2D materials database: high-throughput modeling and discovery of atomically thin crystals. *2D Mater.* **5**, 042002, https://doi.org/10.1088/2053-1583/aacfc1 (2018).
23. Wu, Y.-L., Yang, Q., Geng, H.-Y. & Cheng, Y. The thermoelectric properties of CdBr, CdI, and Janus Cd_2Br I monolayers with low lattice thermal conductivity. *Phys. Chem. Chem. Phys.* **26**, 6956–6966. https://doi.org/10.1039/D3CP05613A (2024).
24. Shafique, A. & Shin, Y.-H. Thermoelectric and phonon transport properties of two-dimensional IV-VI compounds. *Sci. Rep.* **7**, 506. https://doi.org/10.1038/s41598-017-00598-7 (2017).
25. Gjerding, M. N. et al. Recent progress of the computational 2D materials database (C2DB). *2D Mater.* **8**, 044002, https://doi.org/10.1088/2053-1583/ac1059 (2021).
26. Wang, G. et al. Boosting the thermoelectric properties of layered $SnSb_2Te_4$ compound by microstructure regulation combined with heterovalent halogen substitution. *Ceram. Int.* **50**, 25771–25778. https://doi.org/10.1016/j.ceramint.2024.04.313 (2024).

27. Wang, Y., Gao, Z. & Zhou, J. Ultralow lattice thermal conductivity and electronic properties of monolayer 1T phase semimetal $SiTe_2$ and $SnTe_2$. *Physica E: Low-dimensional Systems and Nanostructures* **108**, 53–59. https://doi.org/10.1016/j.physe.2018.12.004 (2019).
28. Kimberly, T. Q., Ciesielski, K. M., Qi, X., Toberer, E. S. & Kauzlarich, S. M. High thermoelectric performance in 2D $Sb2Te_3$ and Bi_2Te_3 nanoplate composites enabled by energy carrier filtering and low thermal conductivity. *ACS Applied Electronic Materials* **6**, 2816–2825. https://doi.org/10.1021/acsaelm.3c00385 (2023).
29. Seredyński, B. et al. Molecular beam epitaxy of a 2D material nearly lattice matched to a 3D substrate: $NiTe_2$ on GaAs. *Cryst. Growth Des.* **21**, 5773–5779. https://doi.org/10.1021/acs.cgd.1c00673 (2021).
30. Bykov, M. et al. High-pressure synthesis of Dirac materials: layered van der Waals bonded BeN_4 polymorph. *Phys. Rev. Lett.* **126**, 175501. https://doi.org/10.1103/PhysRevLett.126.175501 (2021).
31. Tromer, R. M., Pereira, L. F. C., Ferreira, M. & da Luz, M. A direct approach to calculate the temperature dependence of the electronic relaxation time in 2D semiconductors from Boltzmann transport theory. *J. Appl. Phys.* **131**, https://doi.org/10.1063/5.0080938 (2022).
32. Tromer, R. et al. Lattice thermal conductivity of 2D nanomaterials: A simple semi-empirical approach. *Phys. Chem. Chemi. Phys.* **25**, 28703–28715. https://doi.org/10.1039/D3CP02896H (2023).
33. Madsen, G. K. & Singh, D. J. BoltzTraP. A code for calculating band-structure dependent quantities. *Comput. Physi. Commun.* **175**, 67–71, https://doi.org/10.1016/j.cpc.2006.03.007 (2006).
34. Wang, F. Q., Zhang, S., Yu, J. & Wang, Q. Thermoelectric properties of single-layered SnSe sheet. *Nanoscale* **7**, 15962–15970. https://doi.org/10.1039/C5NR03813H (2015).
35. Li, Y. et al. Ultrahigh seebeck coefficient and thermoelectric power factor in semimetal WTe_2. *Appl. Phys. Lett.* **125** (2024).
36. Xu, B. et al. High figure of merit of monolayer Sb_2Te_2Se of ultra low lattice thermal conductivity. *Comput. Mater. Sci.* **177**, 109588. https://doi.org/10.1016/j.commatsci.2020.109588 (2020).
37. Stewart, J. J. MOPAC: a semiempirical molecular orbital program. *J. Comput. Aided Mol. Des.* **4**, 1–103. https://doi.org/10.1007/BF00128336 (1990).
38. Dutra, J. D. L. et al. Sparkle/PM7 lanthanide parameters for the modeling of complexes and materials. *J. Chem. Theory Comput.* **9**, 3333–3341. https://doi.org/10.1021/ct301012h (2013).
39. Giannozzi, P. et al. Quantum Espresso: a modular and open-source software project for quantum simulations of materials. *J. Phys.: Condens. Matter* **21**, 395502, https://doi.org/10.1088/0953-8984/21/39/395502 (2009).
40. Perdew, J. P., Burke, K. & Ernzerhof, M. Generalized gradient approximation made simple. *Phys. Rev. Lett.* **77**, 3865. https://doi.org/10.1103/PhysRevLett.77.3865 (1996).

Acknowledgements

The authors acknowledge support from the Brazilian agencies FAPDF, CNPq, and CAPES through the grants listed above. Computational resources were provided by the National High-Performance Computing Center in São Paulo (CENAPAD-SP, UNICAMP, project proj960) and the High-Performance Computing Center (NACAD, Lobo Carneiro Supercomputer, UFRJ, project a22002).

Author contributions

RMT: Data curation, Software, Investigation Formal analysis, Writing - Original Draft. IMF: Software, Investigation, Visualization, Writing - Original Draft. GDAN: Investigation, Methodology, Resources, Funding acquisition, Writing - Original Draft. FLLM: Investigation, Methodology, Resources, Funding acquisition, Writing - Review & Editing. MLPJ: Conceptualization, Formal analysis, Validation, Investigation, Resources, Project administration, Funding acquisition, Writing - Review & Editing.

Funding

FAPDF (00193-00001807/2023-16), CNPq (444921/2024-9), and CAPES (88887.005164/2024-00).

Declarations

Competing interests

The authors declare no competing interests.

Additional information

Correspondence and requests for materials should be addressed to M.L.P.J.